

RESEARCH

Open Access



Establishment of a patient-derived 3D in vitro meningioma model in xeno-free hydrogel for clinical applications

Mikkel Schou Andersen^{1,2,3*}, Aaraby Yoheswaran Nielsen⁴, Martin Wirenfeldt^{3,5,6}, Jeanette Krogh Petersen⁷, Morten Winkler Møller^{1,2,3}, Christopher L. Powell⁸, Anavaleria Castro^{8,9}, Grayson Herrgott⁸, Tiit Mathiesen^{10,11,12}, Charlotte Aaberg Poulsen⁴, Birgitte Brinkmann Olsen^{4,13}, Henning Bünsow Boldt⁷, Christian Bonde Pedersen^{1,2,3}, Bo Halle^{1,2,3} and Frantz Rom Poulsen^{1,2,3}

Abstract

Background Meningiomas exhibit a complex biology that, despite notable successes in preclinical studies, contributes to the failures of pharmaceutical clinical trials. Animal models using patient tumor cells closely mimic in vivo conditions but are labor-intensive, costly, and unsuitable for high-throughput pharmaceutical testing. In comparison, monolayer cell models (two-dimensional, 2D) are cost-efficient but lack primary tumor cell-cell interactions, potentially overestimating treatment effects. Three-dimensional (3D) models offer an alternative through more precise mimicking of tumor morphology and physiology than 2D models and are less costly than in vivo methods. Here, we aimed to establish a 3D cell model in a solid xeno-free medium using patient-derived tumors, thus creating a bench-to-clinic pathway for personalized pharmaceutical testing.

Methods Four WHO grade 1 and one WHO grade 2 (third-passage, fresh) and 12 WHO grade 1 patient-derived meningioma cells (sixth-passage, frozen) and the malignant IOMM-Lee cell line were used to establish 2D and 3D models. The 3D model was developed using a solid xeno-free medium. After 3 months for the primary tumor and 13 days for the IOMM-Lee cell line, the 3D models were extracted and assessed using histology, immunohistochemistry, and epigenetic analyses (EPICv2 array) on five pairs to evaluate their structural fidelity, cellular composition, and epigenetic landscape compared to the original tumor.

Results None of the frozen samples successfully generated 3D models. Models from fresh meningioma samples were more immunohistochemically similar to the primary tumors compared to 2D models, particularly regarding proliferation. 3D models displayed loss of fibrous tissue. All 3D models had similar copy number variation profiles, visually. Genome-wide DNA methylation level patterns were similar between pairs of 3D models and primary tumors. Correlation plots between CpG methylation levels showed high congruency between primary meningiomas and their corresponding 3D models for all samples ($R > 0.95$).

*Correspondence:
Mikkel Schou Andersen
Mikkel.c.schou.andersen@rsyd.dk

Full list of author information is available at the end of the article



© The Author(s) 2025. **Open Access** This article is licensed under a Creative Commons Attribution-NonCommercial-NoDerivatives 4.0 International License, which permits any non-commercial use, sharing, distribution and reproduction in any medium or format, as long as you give appropriate credit to the original author(s) and the source, provide a link to the Creative Commons licence, and indicate if you modified the licensed material. You do not have permission under this licence to share adapted material derived from this article or parts of it. The images or other third party material in this article are included in the article's Creative Commons licence, unless indicated otherwise in a credit line to the material. If material is not included in the article's Creative Commons licence and your intended use is not permitted by statutory regulation or exceeds the permitted use, you will need to obtain permission directly from the copyright holder. To view a copy of this licence, visit <http://creativecommons.org/licenses/by-nc-nd/4.0/>.

Conclusions Our patient-derived 3D meningioma models closely mimicked primary tumors in terms of cell morphology, immunohistochemical markers and genome-wide DNA methylation patterns, providing a cost-effective and accessible alternative to in vivo models. This approach has the potential to facilitate personalized treatment strategies for patients requiring additional therapy beyond surgery.

Keywords Meningioma, 3D model, Organoid, In vitro model, DNA methylation, Immunohistochemistry, Personalized model, Personalized medicine

Background

Personalized medicine is based on the need to abandon the “one size fits all” approach to diagnostics, drug therapy, and prevention and instead embrace the opportunity of an individualized strategy [1]. Personalized treatment involves identifying specific molecular targets and implementing pre-clinical models that use the patient’s own tumor sample. This approach is expected to significantly enhance the likelihood of therapeutic success. Consequently, there is a critical need for models that closely replicate the unique characteristics of an individual patient’s tumor.

Meningiomas originate from the leptomeninges, which have both mesodermal and neural crest origins [2], and are predominantly benign tumors [3]. They are the most common primary tumors of the central nervous system, accounting for approximately 40% of all primary central nervous system tumors [4]. The incidence is 1.9 per 100,000 for men and 4.5 per 100,000 for women [5, 6]. Meningioma diversity is reflected through the 15 identified histological subtypes [7, 8] that encompass a wide range of specific genetic and epigenetic profiles [9–17].

Surgical intervention remains the primary approach to meningioma treatment [18]. Due to their location, however, not all meningiomas (one-third of skull base tumors) can be fully removed without unacceptable risks [19] to the patient, emphasizing the need for non-surgical treatments. Despite significant efforts, no single pharmaceutical compound has proven universally effective for meningioma treatment [20], and it is more probable that specific subgroups require targeted treatments. Pre-treatment screening for potential effects in individual patients could be useful and relies on a variety of preclinical models, with animal models being the most effective at replicating natural tumor conditions [21]. However, pharmaceutical testing in animal models remains both costly and labor-intensive, making them impractical for large-scale, individualized screenings. This highlights the need to reassess and optimize models for evaluating drug effects in individual meningiomas.

Traditionally, in vitro pharmaceutical testing utilizes two-dimensional (2D) monolayer cell models that are simple and cost-effective but fail to sufficiently mimic in vivo conditions. These models lack the structural complexity of tumors and significantly underrepresent cell-cell and cell-extracellular matrix interactions. This

limitation can influence key cellular processes such as differentiation, proliferation, viability, gene and protein expression, responsiveness to stimuli, and drug metabolism, among other essential functions [22].

Recent advancements in three-dimensional (3D) culture technologies, such as the development of organoids and spheroids, have addressed some of the limitations of traditional 2D monolayer models [22]. The 3D models more accurately replicate the dimensionality, structure, and function of tumors or organs and closely mimic primary patient-derived tumors in terms of morphology, immunohistochemistry, function, and epigenetics [23–29]. Various methods can be employed to establish these models [23]. Spheroids are typically formed through cell aggregation in low-adhesion flasks using simple cell types, whereas organoids derived from stem or tumor cells require more time (up to 2–3 months) to develop their complex structures [23]. Compared with in vivo animal models, 3D models are significantly more cost-effective and accessible, making them promising tools for large-scale identification of potential treatment options.

Through a systematic search of the current literature on 3D models in meningiomas, we identified two studies, which utilized similar methods to create 3D models embedded in a solid medium (Matrigel) using passage 0 cell culture [30, 31]. Despite their methodological similarity, the studies reported differing outcomes, including variations in 3D morphology and success rates of 62.5% [31] and 100% [30]. This indicates a need for further exploration and refinement of these techniques to develop reliable and reproducible 3D models of meningiomas.

The current study aimed to compare the morphological, immunohistochemical, and epigenetic profiles of primary patient-derived meningiomas and their corresponding 3D in vitro models, as well as the morphological and immunohistochemical characteristics across 2D, 3D in vitro, and in vivo models of a commercially available malignant meningioma cell line.

Materials and methods

Patient inclusion and meningioma tissue handling

The study was approved by the Regional Committees on Health Research Ethics for Southern Denmark (S-20190105) and was conducted in accordance with the latest version of the 1964 Declaration of Helsinki.

Informed consent was obtained from all participants, and no identifiable personal details are included. Meningioma (MNG) tissue samples were collected during surgery from patients ≥ 18 years with primary MNG confirmed radiologically and histologically before final enrollment. Samples were transferred to Dulbecco's Eagle Medium (DMEM AQ)(Sigma/D0819) supplemented with 10% fetal bovine serum (FBS) (ThermoFisher/10500064), 1% Penicillin/Streptomycin (ThermoFisher/15140122), 4 mM GlutaMax (ThermoFisher/35050038; stable glutamine), 1 mM Sodium Pyruvate (ThermoFisher/11360039). The whole tumor pieces were washed twice in PBS (ThermoFisher/10140169). The tissue was then mechanically dissociated with scalpels to approximately 1 mm³. The dissociated pieces were resuspended in complete medium in T75 flasks and were incubated at 37C⁰/5% CO₂ for three passages. Medium was changed every 2–3 days. After three passages and at a confluence of app. 70%, cells were trypsinized using TrypLEExpress (ThermoFisher/12605028) and washed twice with PBS. A sample of the cells was embedded in a fibrin clot (mixture of equal part plasma and thrombin).

3D model establishment from fresh third-passage cells

Third-passage cells from primary samples were counted using Nucleocounter (Chemometec A/S, Allerød, Denmark) after adding lysis buffer (buffer A100, 910-0003, Chemometec A/S, Allerød, Denmark), stabilizing buffer (buffer B, 910-0002, Chemometec A/S, Allerød, Denmark) and cells in equal volumes. Xeno-free bio-functional hydrogel (VitroGel ORGANOID-3, VHM04-3, TheWell Bioscience, North Brunswick, NJ, USA) was used to establish 3D models. Briefly, in accordance with the manufacturer's instructions, cells were mixed with hydrogel in 1:2 ratio and were dispersed in 24-well plates with 300 μ l per well in concentrations 5,000 cells/well and 10,000 cells/well. Prior experiments with cells between 1,000 and 60,000 cells/well had been performed to establish the concentrations.

3D model establishment from frozen cell samples

Third-passage cells, frozen in 90% FBS and 10% DMSO from benign primary patient-derived cells, were thawed by centrifuging at 180 g for 5 min, and then resuspended in complete medium in T75 flasks. Cells underwent similar treatment as described above, up to an additional three passages to the sixth passage, where 3D model establishment protocol as described above was performed.

Preparation for histological and immunohistochemical analyses and DNA methylation

3D primary MNG models were extracted after three months. According to the manufacturer's instructions,

3D cell cultures were extracted from the xeno-free hydrogel using VitroGel Organoid Recovery Solution (TheWell Bioscience, North Brunswick, NJ, USA). In brief, hydrogels were extracted from the wells with a spatula and mixed with 37C⁰ recovery solution in conical tubes. The hydrogel was dissolved with gentle rocking. Samples were then spun down at 180 g/5 min. A part of the samples was embedded in fibrin clots as described above for histology and immunohistochemistry, and a part of the 3D models were frozen in 10% DMSO/90% FBS and stored at -80 C⁰ until DNA extraction. All fibrin clot samples were cut into 3 μ m sections on a microtome. Stainings for Hematoxylin & Eosin (H&E), epithelial membrane antigen (EMA), somatostatin receptor type 2 (SSTR2), progesterone receptor (PR), glialfibrillary acidic protein (GFAP), and proliferation marker Ki-67 were performed using the same methods and identical reagents as previously [32]. Tumor pieces were taken directly from surgery and were immersion fixed in 4% neutral-buffered formaldehyde for 24 h prior to being paraffin-embedded and received the same staining as described above.

Histological and immunohistochemical scoring and assessment

The stained slides were digitalized using the NanoZoomer 2.0 digital image scanner (Hamamatsu photonics, Japan) and assessed by two trained neuropathologists (MW and JKP). Disagreements were discussed post priori to reach consensus. During the evaluation process, the neuropathologists were unaware of each other's classifications regarding the MNG subtype and the immunohistochemical staining scores (0, +1, +2, +3), where 0 represented no staining, +1 indicated weak staining, +2 denoted moderate staining, and +3 indicated strong staining. If the assessors' evaluations differed by no more than a single grade (e.g., a score of +2 versus +3 or +1 versus +1), their ratings were considered to be in agreement. In cases of such minor variation, the scores were reported as a range (see Results). All disagreements—defined as differences greater than one grade (e.g., a score of +1 versus +3)—were resolved through a consensus meeting between the neuropathologists. Ki-67 findings from primary tumors, brain sections, and implanted cells were displayed as a range from min to max of both assessors. Ki-67 highest score was also noted representing areas of so-called “hot spots”. Any other differences in grading were resolved through a consensus meeting between the neuropathologists. Both individual and consensus scores can be found in Supplemental Material 1. Sizes were estimated based on brightfield images as 3D models based on fresh patient-derived tumors fragmented upon retrieval from the culture.

3D modelling with a malignant cell line

The malignant cell line was purchased from American Type Culture Collection (ATCC) (CRL-3370) and was acquired in September 2022 (IOMM-Lee Meningioma Human, LOT: 70027737, authenticated by ATCC). IOMM-Lee originates from a frontal tumor in a 61-year-old male [33] and is the most commonly used commercially available cell type in MNGs preclinical research. The original stock (which was mycoplasma-free) was incubated for three passages and refrozen in multiple vials. Adherent/monolayer 2D cells were incubated as described above. The 3D model was established with the same stock of third-passage cells used for *in vivo*. Various concentrations from 1,000 to 10,000 were tested prior, and 1,000 cells/well were chosen based on growth potential assessed through brightfield microscopy and basic histology with H&E sections. 3D model experiments incubated for a couple of weeks to match *in vivo* incubation period and received similar stainings as described above.

In vivo modelling with a malignant cell line

To assess *in vitro* and *in vivo* differences in morphology and immunohistochemistry, we established an orthotopic model in two Crl: NIH-Fox1rnu athymic, female nude rats homozygous, 5–7 weeks old at implantation (Charles River Laboratories, Germany) after one week of acclimatation, using 100,000 and 250,000 cells harvested from the 2D adherent monolayer culture using an identical method as published before by our group through superficial injection via a burr hole in front of bregma to the right [32]. Animal experiments were approved by the Danish Animal Experiments Inspectorate (2019-15-0201-00195), and all experiments were conducted in accordance with local guidelines, national regulations, the Danish 3R-Center and to the Principles of Laboratory Animal Care (NIH publication No. 86–23, revised 1985). For detailed description of the experimental setup, which followed the ARRIVE 2.0 the recommended set [34] for animal experiments, see Supplemental Material 5. Animals were terminated after a couple of weeks (13 days) based on the findings from a systematic review from our group [21] and received similar stainings as described above.

Assessment of 3D models with similar methods in a systematic literature search

The systematic literature search for a scoping review on 3D models in MNGs (in preparation) included the databases Embase, Medline, and Web of Science. The scoping review protocol was published on the first author's personal page on ResearchGate.net. In compliance with PRISMA Extension for Scoping Reviews (PRISMA-ScR Check) [35], the protocol, is also available

as Supplemental Material 6. The literature search strings from two rounds are available in Supplemental Material 7 and 8. All records extracted were screened by two of the authors (MSA + AYN). All records deemed eligible by either of the authors in the first round of screening were included in the second round. Inter-rater agreement using Cohen's Kappa statistics [36] was 0.85 after initial screening.

DNA methylation Preparation

Formalin-fixed, paraffin-embedded (FFPE) sections from primary tumors were cut into 10 μm slices (two or three per sample) and underwent DNA extraction following the QIAamp DNA FFPE Tissue Kit protocol (QIAGEN, Germany), as described in Supplemental Material 4. DNA from frozen trypsinized 3D models was extracted using the MagNA Pure 96 System (Roche Diagnostics, Germany) with 200 μL of sample (cells in lysis buffer) and 300 μL of PBS buffer, totaling 500 μL per well. The MagNA Pure 96 DNA and Viral NA Large Volume Kit reagents were used following the manufacturer's protocol. The final elution volume was 100 μL , and DNA concentration was measured using a Qubit fluorometer. To ensure consistency, DNA was extracted from both the primary tumors and their corresponding 3D models at the same time point, followed by DNA methylation profiling using the same EPICv2 935 K chip for each of the pairs. Manufacturers' protocols were followed. DNA quality was verified with the Infinium HD FFPE Methylation Assay 2.0 (Illumina Inc., CA, USA). Bisulfite conversion was performed using the EZ DNA Methylation Kit (Zymo Research Corp., CA, USA), and DNA was restored with the Infinium HD Assay Kit FFPE – Restore Kit (Illumina Inc., CA, USA) and the ZR-96 DNA Clean and Concentrator kit (Zymo Research Corp., CA, USA). DNA amplification followed the Infinium HD FFPE Methylation Assay protocol (Illumina Inc., CA, USA). DNA methylation data were obtained via the iScan System (Illumina Inc., CA, USA).

Unsupervised and supervised analysis of DNA methylation levels

Raw IDAT files were processed through the DNA methylation-based CNS classifier [37] to evaluate copy number variation and classifications using the Brain Tumor Classifier (v12.8).

Genomic methylation analyses were performed in R (v 4.4.1) with Bioconductor (v 3.20) using Minfi (v 1.52.1) for analyzing and visualizing DNA methylation data. Minfi's 'preprocessingIllumina' was utilized for initial processing of the probes. Probes with a detection of $P > 1.0 \times 10^{-16}$ in any sample were filtered out, and quality control of the probe set was run with the 'getQC' function (cutoff set to 11). Duplicate/replicate probes were averaged across

the beta matrix to generate a single beta value per probe. Probes that contained SNPs either at the CpG interrogation or at the single nucleotide as well as all masked probes and probes that were located on the X chromosome or Y chromosome were filtered out ($n=39811$ removed probes for 10-sample set, and $n=39797$ probes for 8-sample set) (a complete list of masked probes is provided by Zhou et al. [38]). The 8-sample set included MO-38 to MO-41 both tumors and 3D models, and the 10-sample set also included MO-42. The final unmasked beta matrix probe count after preprocessing and filtering was 867101 probes for the 10-sample set and 867115 probes for the 8-sample set. The top 1,000 most variant CpG sites were selected across all samples, and heatmaps were generated using the ComplexHeatmap package [39]. We performed 3D principal component analysis (PCA) for dimensionality reduction and visualization. Correlation plots were generated for each of the primary tumors and their corresponding 3D model, focusing on CpGs from the whole genome of the 10-sample set. Pearson's correlation statistic was used to determine statistical significance for the correlation plots. Comparison of probes between primary patient-derived tumors and 3D models was completed through pairwise comparisons (Wilcoxon rank-sum test). Differentially methylated probes (DMPs) were defined using p -values adjusted for false discovery rate (FDR) and the mean methylation difference (diff.mean) between groups. Throughout the analyses we found no significant adjusted p -values, hence all DMP analyses was performed on raw p -values. Additionally, traditional significance levels for unadjusted p -values ($p_{\text{raw}} \leq 0.05$) and cutoffs of $\text{diff.mean} > 0.2$ and > 0.4 were used as baselines to define significant DMPs.

Functional gene enrichment analysis

Gene set enrichment analysis (GSEA) was performed to evaluate the top 20 pathways associated with genes linked to the most significant differentially hypomethylated and hypermethylated DMPs between the tumor/3D MNG pairs ($p_{\text{FDR}} \leq 0.05$; $\text{abs}(\text{diff.mean}) \geq 0.4$) using the Molecular Signatures Database (MsigDB) via Gene Set Enrichment Analysis (GSEA) from the Broad Institute [40]. The analysis was conducted using canonical pathway sets (BioCarta, KEGG, PID, Reactome, WikiPathway) and ontological gene sets (GO: BP, GO: MF, GO: CC) for comprehensive insights.

Genes were annotated via an in-house script that reads in both the Infinium MethylationEPIC GenomeStudio V2.0 manifest file [41] (v2.0 A2) and the Gencode Release 47 (GRCh38.p14) comprehensive gene annotation file. The EPIC V2.0 manifest file was subsetted to include only 'cg' probe type and to remove any probes that were labeled as located on chromosome '0'. These probes either lack a reliable mapping or have multiple mappings that

are statistically the same. Duplicate probes were collapsed into a single probe name while keeping each of the unique Illumina names. The Gencode file was subsetted to genes only, and gene ranges were generated via the 'Granges' package. When mapping the EPIC V2.0 manifest with the Gencode file, strand was accounted for ($\text{ignore.strand} = F$).

Results

Clinicopathological characteristics of included samples

We included MNG tissue sample from 18 patients in this study. The fresh sample group consisted of five primary patient-derived samples, while 12 samples were obtained from frozen third-passage cells derived from 12 patients. Additionally, one malignant sample was included from the commercially available malignant MNG cell line, IOMM-Lee [33]. Of the five fresh primary patient-derived tumors, four were classified as WHO grade 1 MNGs and one as WHO grade 2 according to the 2021 WHO guidelines [7]. All frozen primary tumors were benign WHO grade 1.

All five fresh samples, as well as the malignant IOMM-Lee cell line, developed into 3D cell cultures within the hydrogel. In contrast, none of the 12 third-passage frozen MNG samples formed 3D cultures and instead exhibited signs of cell death under brightfield microscopy. Table 1 provides an overview of the sample characteristics.

3D model cell morphology resembles primary meningioma cells

Three primary samples were WHO-grade 1, meningothelial subtype with lobulated architecture and focally whorled growth pattern (MO-38, MO-39, and MO-42). The tumor cells were epithelioid cells with round to oval nuclei without mitotic activity. MO-39 primary tumor displayed some pseudoinclusions, and MO-42 only displayed a discrete whorled growth pattern. However, the tumor cells showed an abundant syncytia-like cytoplasm with small oval nuclei and indistinct nucleoli. The remaining two primary samples (MO-41, grade 1 and MO-40, grade 2) had fascicular growth pattern and tumor cells in a fibrous collagen matrix consistent with fibrous MNGs. MO-40 tumor cells were blunt to spindle-shaped with oval to irregular nuclei, and some showed pseudoinclusions and invasive brain growth. For all 2D meningeal tumor cells from monolayer culture coalesced in fibrin clots, single tumor cells varied in shape, size, and nuclear morphology, and some nuclei had quite prominent nucleoli. 3D models fragmented upon retrieval from the culture, but all had clear MNG cell morphology. Cells were coalesced in fibrin clots, and individual tumor cells were rounded to slightly elongated. The growth pattern of MO-39 resembled the primary tumor, but there were no nuclear holes or pseudoinclusions. Cells from MO-40

Table 1 Clinicopathological characteristics of primary meningioma samples that underwent cell culture

Sample	Type	Age	Sex	Location	WHO-grade	Tumor subtype	3D success?
MO-38	Fresh	70	Female	Olfactory	Benign – 1	Meningothelial	Yes
MO-39	Fresh	72	Male	Frontal falx	Benign – 1	Meningothelial	Yes
MO-40	Fresh	59	Female	Sphenoid wing	Atypical – 2	Fibrous	Yes
MO-41	Fresh	49	Female	Frontal falx	Benign – 1	Fibrous	Yes
MO-42	Fresh	40	Female	Convexity	Benign – 1	Meningothelial	Yes
IOMM-Lee	Stock	60	Male	Frontal	Malignant – 3	Anaplastic	Yes
MO-4	Frozen	63	Female	Sphenoid wing	Benign – 1	Transitional	No
MO-6	Frozen	69	Female	Frontal falx	Benign – 1	Meningothelial	No
MO-7	Frozen	76	Female	Sphenoid wing	Benign – 1	Meningothelial	No
MO-12	Frozen	72	Female	Convexity	Benign – 1	Microcystic	No
MO-14	Frozen	69	Male	CP angle	Benign – 1	Transitional	No
MO-15	Frozen	72	Female	Frontal falx	Benign – 1	Angiomatous	No
MO-17	Frozen	54	Male	Convexity	Benign – 1	Meningothelial	No
MO-18	Frozen	40	Female	Parietal falx	Benign – 1	Transitional	No
MO-20	Frozen	56	Male	Olfactory	Benign – 1	Transitional	No
MO-22	Frozen	42	Male	Sphenoid wing	Benign – 1	Meningothelial	No
MO-25	Frozen	64	Female	Frontal falx	Benign – 1	Transitional	No
MO-27	Frozen	80	Female	Olfactory	Benign – 1	Fibrous	No

Notes: MO: Meningioma Odense, CP angle: Cerebellopontine angle

were similar to the primary tumor with an irregular morphology. Collagen or fibrous tissue did not translate to in vitro conditions. MO-42 nuclei were oval and quite uniform in shape and size like the corresponding primary tumor (Fig. 1). For closer evaluation of morphological descriptions, see Supplemental Material 3.

The IOMM-Lee malignant 3D cell model did not fragment as the benign and atypical primary patient-derived models did upon extraction from the hydrogel. In monolayer culture, these tumor cells exhibited some variation in shape (irregular), size, and nuclear morphology, with some nuclei having nucleoli. Cell morphology was also preserved in the 3D and in vivo samples, which showed no specific growth patterns. The 3D model overall histological morphology somewhat resembled the in vivo xenografts. The nuclei varied in both shape and size with less prominent nucleoli compared to the in vivo xenograft (Fig. 2).

Sizes (diameter) for all 3D model primary patient-derived samples ranged from 50 to 200 μm (MO-38: approx. 50–100 μm , MO39: approx. 200 μm , MO-40: 80–150 μm , MO-41: 50–100 μm , MO-42: 150 μm) (Fig. 1). The diameters of the malignant IOMM-Lee 3D models were estimated to 100–300 μm (Fig. 2).

Immunohistochemical congruency with minor differences between primary tumor and 3D models

Overall, primary tumors and IOMM-Lee samples displayed similar immunohistochemical profiles to their corresponding 3D models with slight differences (Figs. 1 and 2, and Table 2).

The cytoplasmatic stainings of EMA, SSTR2, and GFAP showed congruency between primary tumors and 3D models to some degree. EMA expression was regained in 3D for two samples (MO-38 and MO-42) (primary patient-derived tumor ($PPDT$) > 2D and $PPDT = 3D$ staining intensity) and showed similar staining in three samples (MO-39, MO-40, and MO-41) ($PPDT$ > 2D and $2D = 3D$ staining intensity). 2D models displaying lower staining intensity for all. SSTR2 expression was more heterogenous from primary tumors to 3D models but showed similar expression from 2D to 3D in most of the samples (MO-38, MO-40, MO-41) ($PPDT$ (>) 2D + 3D, $2D = 3D$ staining intensity); the corresponding primary tumors stained more strongly overall. Lastly, the cytoplasmatic staining of GFAP showed consistent non-specific staining from primary tumor to 2D to 3D. PR expression was either nearly lost or lost already in the third-passage 2D cells (MO-38 and MO-40). Here the primary tumors showed poor expression (+1/+2). Two samples showed retained PR expression throughout primary tumor to 2D to 3D (MO-39 and MO-42). Proliferation marker Ki-67 displayed comparable values for primary tumors and 3D models (1–20%). In general, Ki-67 was much higher in the third-passage 2D cells in all samples except MO-40 primary tumor, 2D and 3D that had comparable Ki-67 levels (Fig. 1).

Ki-67 proliferation marker in the malignant cell line IOMM-Lee showed a higher percentage for 2D grown cells (95–100%) compared to in vivo (75–90%) and 3D (50–90%). Remaining immunohistochemistry staining scores were either 0 (EMA, SSTR2, and PR) or stained non-specifically (GFAP) (Fig. 2).

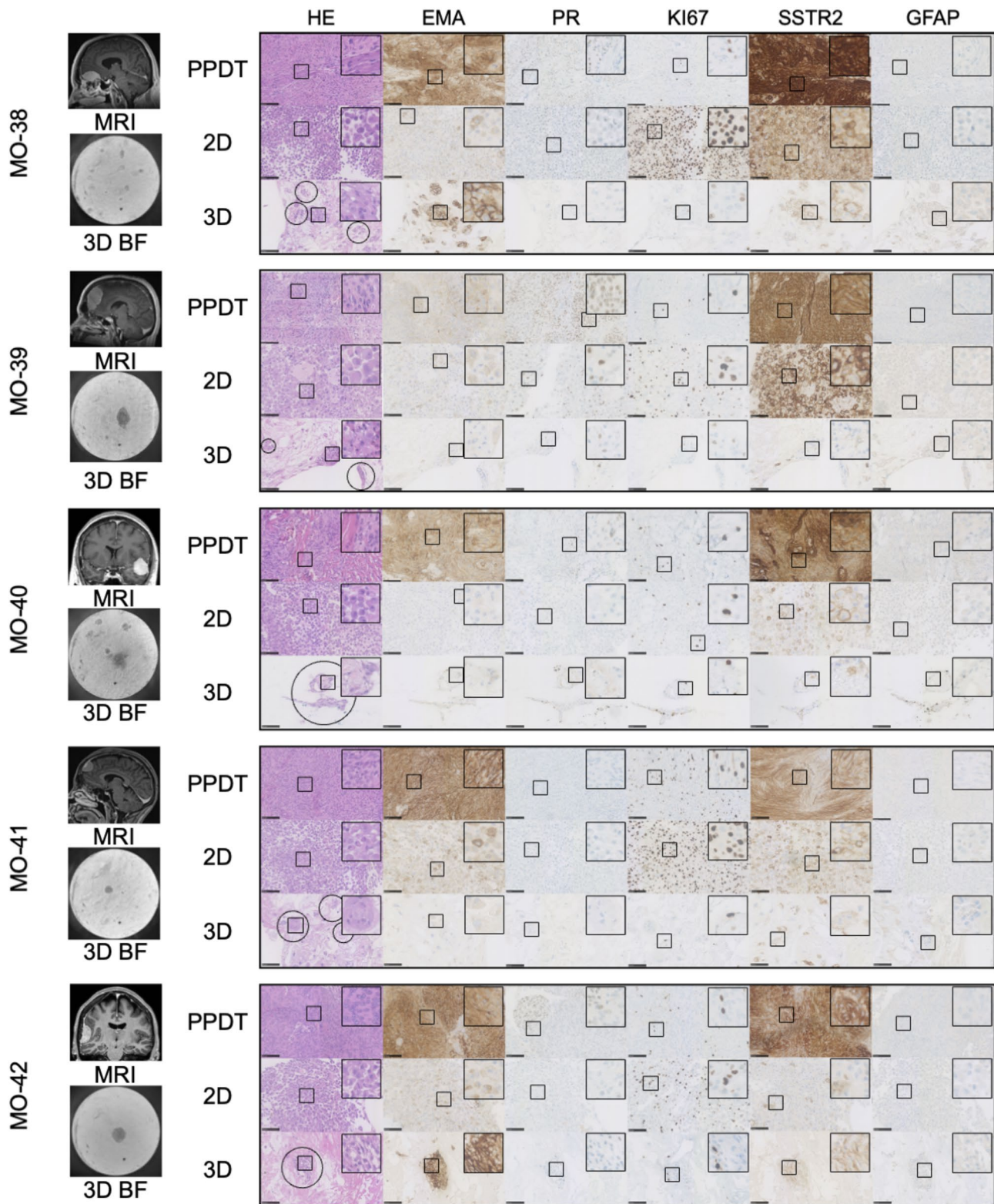


Fig. 1 Histology and immunohistochemistry of primary patient-derived meningiomas (tumors) (PPDT)/primary tumors and corresponding 2D and 3D models – Representative images. 3D models were incubated for 3 months. Representative images of magnetic resonance images (T1-weighted) of the primary tumors can be seen to the left (See Table 1 for clinicopathological characteristics). **3D BF**: 3D brightfield, the field of view (circle) is 1 mm/1000 μ m in diameter – used to estimate 3D model diameters. **PPDT**: primary patient-derived tumor, **2D**: monolayer cell model embedded in fibrin clots, **3D**: 3D models embedded in fibrin clots **H&E**: Hematoxylin and Eosin, **EMA**: Epithelial membrane antigen, **PR**: Progesterone receptor, **Ki-67**: Proliferation, **SSTR2**: Somatostatin receptor 2, **GFAP**: Glial fibrillary acidic protein. **Black scale bars**: All histology slides: 100 μ m

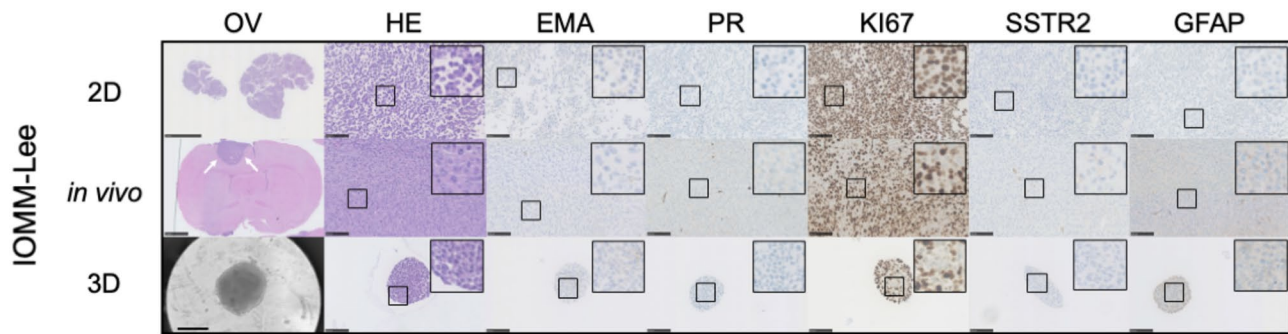


Fig. 2 Histology and immunohistochemistry of IOMM-Lee monolayer third-passage 2D model, xenograft (in vivo), and 3D model – Representative images. Both the in vivo and the 3D models were incubated for 13 days. **H&E**: Hematoxylin and Eosin, **EMA**: Epithelial membrane antigen, **PR**: Progesterone receptor, **Ki-67**: Proliferation, **SSTR2**: Somatostatin receptor 2, **GFAP**: Glial fibrillary acidic protein. **Black scale bars**: All histology slides: 100 μ m. The overview (**OV**) images represent 2D: overview of fibrin clots black bar: 2,5 mm. in vivo: Coronal slice of rat brain with white arrows pointing towards tumor, black scale bar: 2,5 mm. **3D**: 3D brightfield, the circle is 1 mm in diameter – black scale bar represent 200 μ m

Table 2 Immunohistochemical staining showing semiquantitative scores across primary tumors and corresponding 2D and 3D models

Sample	Type	EMA	PR	Ki-67	SSTR2	GFAP	BC Overall	BC Best subclass	
MO-38	T	+3	+1+2	5%(10%)	+3	NS	MNG: 0.99	Ben: 0.99	2: 0.91
	2D	+1	0+1	95%(100%)	+2+3	NS	NA	NA	NA
	3D	+3	0	5%(10%)	+2	NS	MNG: 0.98	Ben: 0.77	2: 0.76
MO-39	T	+1+2	+2+3	2–5%(20%)	+3	NS	MNG: 0.99	Int: 0.76	A: 0.76
	2D	+1	+2	15–30%	+3	NS	NA	NA	NA
	3D	0+1	+1	2–5%	0+1	NS	MNG: 0.98	Ben: 0.91	1: 0.46
MO-40	T	+3	+1	2–10%(20%)	+2+3	NS	MNG: 0.99	Ben: 0.99	1: 0.99
	2D	0+1	0	2–10%	+2	NS	NA	NA	NA
	3D	+1	0	1–10%	+1	NS	MNG: 0.99	Ben: 0.98	3: 0.87
MO-41	T	+3	0	15–20%(30%)	+3	NS	MNG: 0.99	Ben: 0.99	1: 0.99
	2D	+2	0	50–70%	+2	NS	NA	NA	NA
	3D	+1	0	10–20%	+1+2	NS	MNG: 0.98	Ben: 0.98	1: 0.98
MO-42	T	+3	+2	5–10%(20%)	+3	NS	MNG: 0.99	Ben: 0.89	2: 0.88
	2D	+1	0+1	20–40%	+1	NS	NA	NA	NA
	3D	+3	+1	5–10%	+2–3	NS	MNG: 0.99	Ben: 0.99	2: 0.96
IOMM-Lee	2D	0	0	95–100%	0	NS	NA	NA	NA
	in vivo	0	0	75–90%	0	NS	NA	NA	NA
	3D	0	0	50–90%	0	NS	NA	NA	NA

Notes: Staining scores: 0 = no staining, +1 = weak staining, +2 = moderate staining, and +3 = strong staining. Scoring values and percentage presented as min to max for both assessors to display the range. Ki-67 is displayed as min-max between the assessors. Ki-67 highest score is shown in parenthesis for areas with a distinctly higher score (so-called “hot spots”). **EMA**: Epithelial membrane antigen; **PR**: Progesterone receptor, **SSTR2**: Somatostatin receptor 2, **GFAP**: Glial fibrillary acidic protein; **NS**: Non-specific; **BC**: Brain Classifier v12.8, **NA**: Not applicable, **MNG**: Meningioma, **Ben**: Benign, **Int**: Intermediate

Further evaluations of the immunohistochemistry of individual 3D models are available in Supplemental Material 1, and examples of scoring are available in Supplemental Material 2 (primary tumors, 2D and 3D models).

Brain Classifier v12.8 results

All samples matched with “meningiomas”. MO-38, MO-41, and MO-42 (all WHO grade 1) matched best with the benign category, showing similar subclasses between the primary tumors and their corresponding 3D models. MO-40 (WHO grade 2) also matched best with

the benign category for both the primary tumor and 3D model, although the subclasses differed. Finally, MO-39 (WHO grade 1) matched best with the intermediate A category in the primary tumor, although the result was not significant (0.76). In contrast, the corresponding 3D model matched best with the benign category (0.91), with subclass 1 being insignificant (0.46) (Table 2).

Epigenetic analyses revealed high congruency between sample pairs

The bisulfite conversion was efficient for all samples. All samples exhibited acceptable DNA quality with a CpG

detection p -value $\geq 99\%$. Preprocessing also revealed high quality DNA (see Supplemental Material 9).

We identified five optimal methylation-based clusters through k -means unsupervised hierarchical clustering and analysis of appropriate consensus measures across the 1000 most variant CpGs, visualizing them through methylation-based heatmaps (beta value). The models and tumors were paired for MO-38 to MO-41, while the 3D model for MO-42 had more in common with the 3D model and primary tumor of MO-40 (see Supplemental Material 10). Heatmap excluding the MO-42 sample showed clusters in pairs despite assessing the top 1000 most variant CpG probes. The heatmap showed some methylation level differences, especially in enhancers in the gene body location—where 3D models were predominantly hypomethylated compared to their corresponding tumors (Fig. 3).

Correlation plots across a subset of the whole genome revealed correlations between $R=0.96$ – 0.99 (MO-38: $R=0.97$, $p < 2.22 \times 10^{-16}$; MO-39: $R=0.98$, $p < 2.22 \times 10^{-16}$; MO-40: $R=0.97$, $p < 2.22 \times 10^{-16}$; MO-41: $R=0.99$, $p < 2.22 \times 10^{-16}$; MO-42: $R=0.96$, $p < 2.22 \times 10^{-16}$) (Fig. 4A). Analysis also revealed the samples were in proximity in the 3D PCA plot (Fig. 4B).

Supervised DNA methylation analysis comparing primary tumors and corresponding 3D models revealed only a small number of DMPs at an unadjusted p -value significance level of $p \leq 0.05$. Overall, the 3D models exhibited predominant hypomethylation compared to primary patient-derived tumors. At a diff.mean cut-off of (0.2) 20%, most CpGs displayed insignificant differences, with 3,900 hypomethylated and 686 hypermethylated probes identified. Application of a stricter diff.mean cut-off at (0.4) 40% to highlight the most significant changes narrowed the findings to 486 hypomethylated and 13 hypermethylated probes (Supplemental Material 11).

3D models recapitulate copy number variation from the primary tumors

Copy number variation profiles showed strong visual similarities between the primary patient-derived tumors and their corresponding 3D in vitro model for all five samples. In general, we detected no chromosomal number alterations from primary tumors to 3D models. MO-38 showed no cytogenetic changes in either the primary tumor or the 3D model. MO-39 displayed loss of chromosomes 14 and 22, both common in MNGs. Loss of 22q (which harbors NF2) was also observed in MO-40

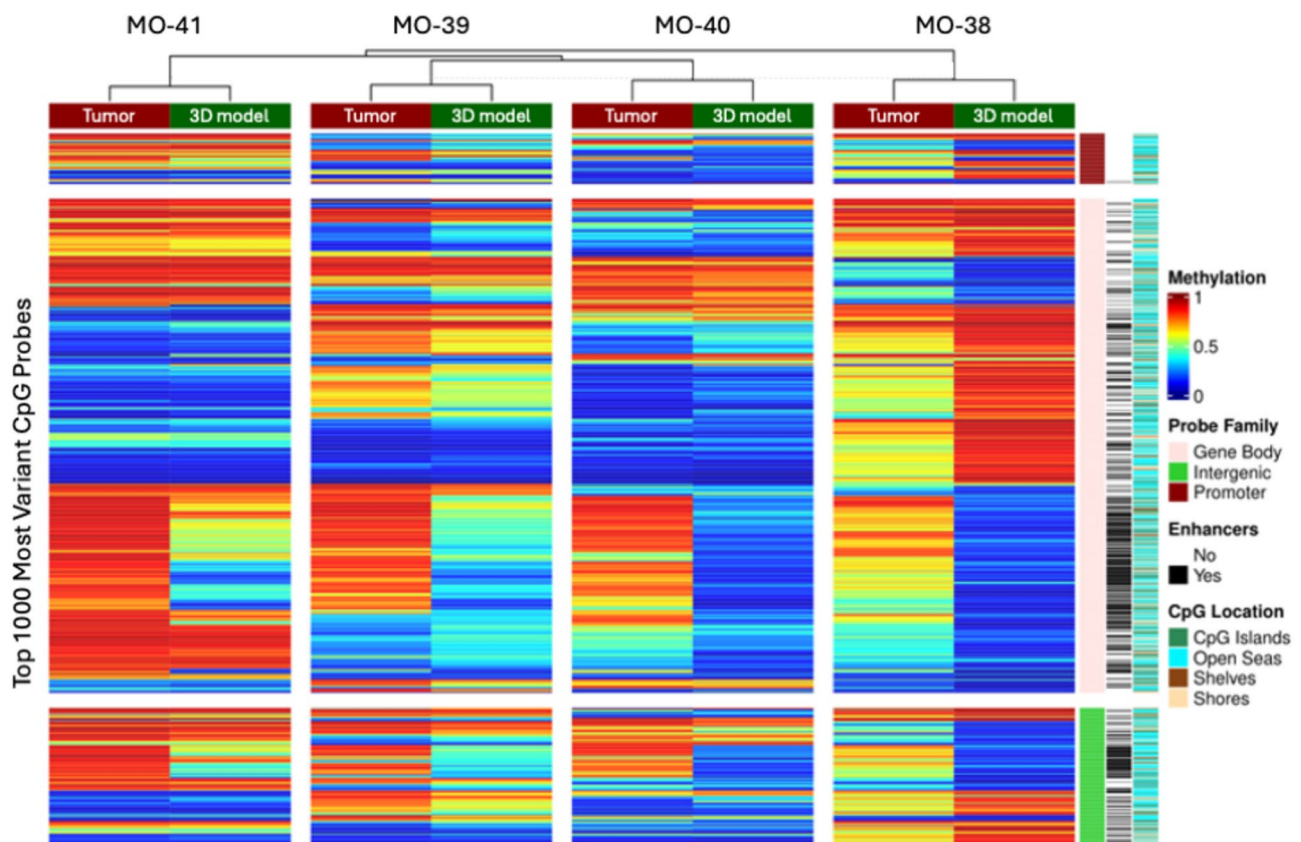


Fig. 3 Heatmap displaying the unsupervised clustering of the top 1000 most variable CpG probes. Methylation heatmap displaying the 1000 most variable methylated probes (beta values) across unsupervised k -clusters ($n=8$ samples). Samples are sorted into methylation-based clusters and annotated by sample type (Tumor, 3D model)

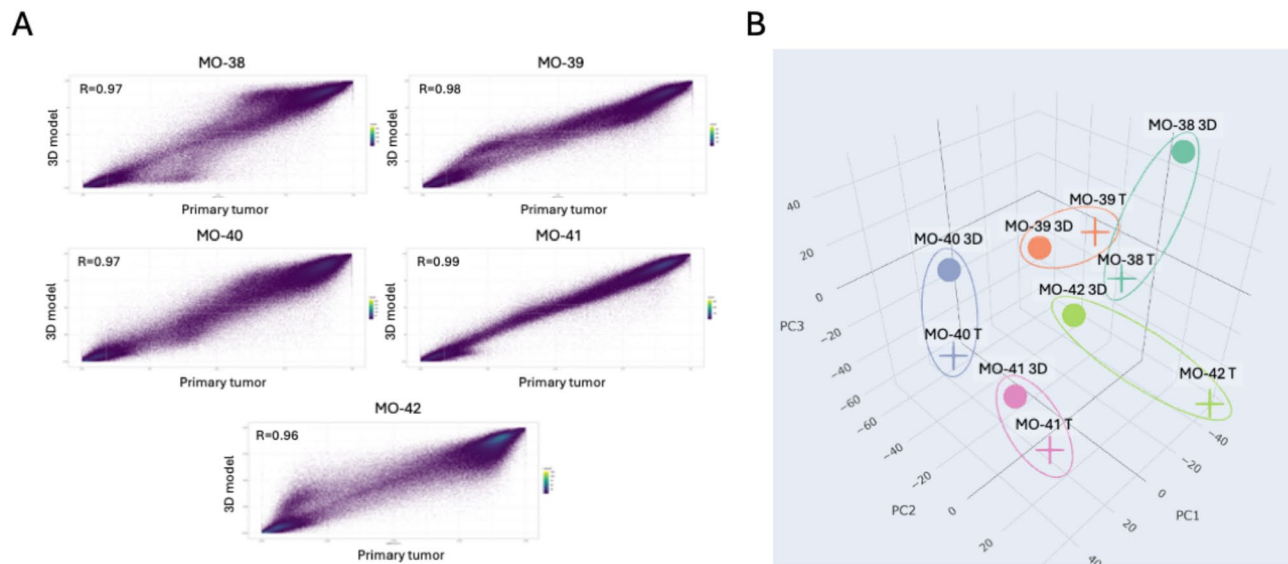


Fig. 4 Correlation plots across 10k probes between tumor and 3D samples from five patients. **(A)** Depicts correlation plots of whole genome hypo- and hypermethylated probes for all five sample pairs. **(B)** Whole genome 3D PCA plot showing how pairs align in a 3D vector environment. Circles depict 3D models, and crosses depict primary patient-derived tumors. Different colors represent different patients

and MO-41 without any other cytogenetic changes. The MO-42 primary tumor showed a more complex profile, with certain gains in chromosomes 3, 5, 8, 9, 10, 12, 13q, 14q, 15q, 17, 20, and 21, which were also observed in the 3D model although at a lower signal intensity. A lower intensity was similarly noted - to a lesser degree - in MO-39 (Fig. 5).

Gene set enrichment analysis

A total of 486 hypomethylated CpG sites (significant DMPs using raw p-values) were identified, of which 249 were associated with genes, and 13 hypermethylated CpG sites were found, of which 10 were linked to genes. The genes were associated with the following areas: (1) cytoskeletal dynamics and cell motility, (2) tissue repair and extracellular matrix remodeling, (3) cell-cell and cell-matrix interactions, (4) developmental processes and plasticity, (5) transcriptional and RNA regulation, and (6) Rho GTPase signaling and projections. No overlaps were identified for hypermethylated probes at this cut-off. For a detailed overview of the pathways, see Table 3, numbers in the text correspond with the numbers in the table. The complete GSEA analysis is available in the Supplemental Material 12.

Discussion

In this study, we successfully developed and established an *in vitro* 3D model using a solid, xeno-free hydrogel. Single-cell suspensions from four WHO-grade 1 and one WHO-grade 2 fresh patient-derived tumors were cultured for three months, while a commercially available WHO-grade 3 cell line (IOMM-Lee) [33] was cultured

for two weeks. Notably, the patient-derived 3D models retained highly conserved characteristics, including histological features, surface marker expression, and epigenetic profiles.

Morphologically, we observed comparable cell types where the 3D models more accurately represented the primary patient-derived cell morphology compared to the corresponding 2D models. However, the overall cytoarchitecture of meningioma subtypes, particularly the fibrous tissue and collagen components, was not retained in the 3D models. Previous literature using a similar method to ours (growth in a solid medium) have reported morphological congruency between primary tumor and 3D model without being described further to allow comparisons between our approaches [30]. Similarly, Chan et al. [31] described the successful development of 3D architectures but did not compare them to the corresponding primary tumors. Their 3D models exhibited extensive areas of sparse cellularity interspersed with clusters of densely packed cells. The malignant cell line exhibited similar cell morphology across 2D, *in vivo*, and 3D models, with a notable resemblance between the 3D and *in vivo* models. This congruency may result from a highly homogeneous cell population maintained over many passages [42], which limits its ability to accurately replicate the complex pathophysiology of meningiomas [21]. However, it underscores the model's capacity to mimic primary samples, as exemplified by the *in vivo* model. Our 3D models show spherical cell models with similar sizes (ranging from 50 to 200 μm) comparable to those of Yamazaki et al. [30]. Immunohistochemically, we found a closer representation of cytoplasmic staining

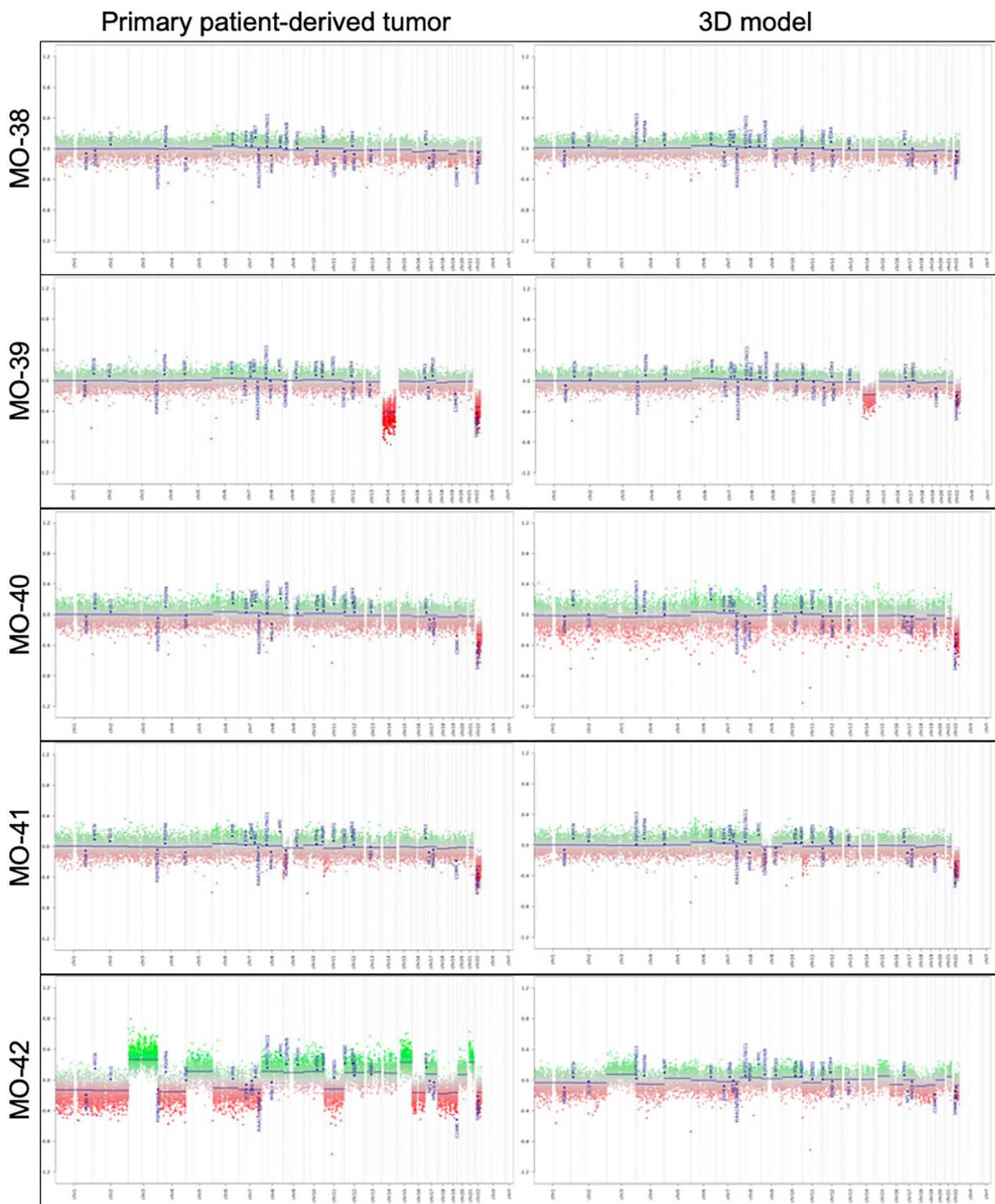


Fig. 5 Cytogenetic analysis of primary tumors and corresponding 3D models - copy number variation (CNV) profiles. No significant changes were observed from the primary patient-derived meningiomas to their corresponding 3D model. However, variations in signal intensity (particularly in complex karyotypes like MO-42) highlight the potential influence of 3D culture conditions on chromosomal patterns

Table 3 Gene set enrichment analysis table for the 20 most significant gene sets based on the 0.4 cut-off analysis

Gene Set Name (All hypomethylated)	Description	# Genes in Overlap	FDR q-value
GOBP_ACTIN_FILAMENT_BASED_PROCESS (1)	Hypomethylation of these genes suggests increased cytoskeletal organization, rearrangement, and actin filament dynamics, leading to enhanced cell motility, structural adaptability, and migration.	20	1.84×10^{-6}
GOBP_CELL_MOTILITY (1)		29	1.84×10^{-6}
GOCC_ACTIN_CYTOSKELETON (1)		13	1.4×10^{-4}
GOMF_CYTOSKELETAL_PROTEIN_BINDING (1)	Enhanced expression of genes encoding cytoskeletal-binding proteins is linked to improved cell shape maintenance, intracellular transport, and mechanical stress response.	18	9.99×10^{-5}
GOBP_RESPONSE_TO_WOUNDING (2)	Hypomethylation highlights the activation of genes driving tissue repair and ECM remodeling, facilitating rapid responses to damage and improved regenerative capacity and maintaining intercellular interactions in both normal and pathological conditions	16	4.86×10^{-6}
GOBP_WOUND_HEALING (2)		13	4.17×10^{-5}
GOBP_POSITIVE_REGULATION_OF_EXTRACELLULAR_MATRIX_ORGANIZATION (2)		5	1.27×10^{-4}
GOBP_POSITIVE_REGULATION_OF_CELL_PROJECTION_ORGANIZATION	Hypomethylation promotes the formation of cellular projections such as filopodia and lamellipodia, enhancing cell motility and migration, critical in processes like metastasis and wound healing.	11	4.16×10^{-6}
GOBP_CELL_JUNCTION_ORGANIZATION (3)	Hypomethylation of genes involved in cell junction formation supports enhanced adhesion and structural coordination, important for tissue stability and function. Upregulation of genes facilitating the assembly of cellular components could strengthen structural stability and adaptability in dynamic environments like 3D cultures.	17	3.28×10^{-5}
GOCC_ANCHORING_JUNCTION (3)		18	4.17×10^{-5}
GOBP_POSITIVE_REGULATION_OF_CELLULAR_COMPONENT_ORGANIZATION (3/6)		22	1.66×10^{-4}
GOBP_MUSCLE_STRUCTURE_DEVELOPMENT (4)	Hypomethylation activates genes required for muscle structure development and differentiation, suggesting a shift towards tissue-specific functional states or increased plasticity in response to environmental (in vitro conditions) or physiological demands.	16	4.7×10^{-5}
GOBP_POSITIVE_REGULATION_OF_DEVELOPMENTAL_PROCESS (4)	Hypomethylation-driven upregulation may indicate enhanced epithelial tissue development, contributing to epithelial-mesenchymal transitions or remodeling processes (plasticity)	21	1.37×10^{-4}
GOBP_EPITHELIUM_DEVELOPMENT (4)		20	1.04×10^{-4}
GOBP_POSITIVE_REGULATION_OF_TRANSCRIPTION_BY_RNA_POLYMERASE_II (5)		22	1.35×10^{-5}
GOBP_POSITIVE_REGULATION_OF_RNA_METABOLIC_PROCESS (5)	Hypomethylation might lead to increased transcriptional activity and RNA metabolism. This aligns with the observation that hypomethylation often removes repressive marks, enabling more active transcription of genes.	26	5.83×10^{-5}
GOBP_LOCOMOTION (1)	Hypomethylation of genes regulating locomotion suggests increased cellular movement and migration, playing a significant role in tissue repair, immune responses, and cancer progression	21	1.04×10^{-4}
GOBP_REGULATION_OF_LOCOMOTION (1)		20	5.83×10^{-5}
GOCC_NEURON_PROJECTION (6)	This indicates that genes involved in the formation, structure, or function of neuron projections (such as axons, dendrites, or other cellular protrusions) are likely upregulated in the 3D cell model.	21	9.85×10^{-5}
REACTOME_SIGNALING_BY_RHO_GTPASES_MIRO_GTPASES_AND_RHOBTB3 (6)	Suggests that hypomethylation activates Rho GTPase-related signaling, which is a key regulator of cytoskeletal dynamics, cell migration, and intracellular trafficking. This pathway likely plays a central role in the structural and motility-related changes observed.	15	1.53×10^{-4}

Notes: Full analyses are available as supplemental material (SM10). Notes: ECM: Extracellular matrix, FDR q-value: False discovery rate q-value. The gene sets can be divided into the following areas: (1) cytoskeletal dynamics and cell motility, (2) tissue repair and extracellular matrix remodeling, (3) cell-cell and cell-matrix interactions, (4) developmental processes and plasticity, (5) transcriptional and RNA regulation, and (6) Rho GTPase signaling and projections

for EMA and SSTR2 between primary tumor and 3D models compared to the 2D models as shown in Fig. 1. In our 3D model, EMA and SSTR2 were either largely regained or comparable to those observed in 2D models. This aligns with findings from other studies on 3D models, where SSTR2 was reported to be highly retained in some cases [30] and less retained in others [43].

Fast-dividing tumor cells have less time for DNA repair, which increases their susceptibility to accumulating damage and triggering apoptosis [44]. Furthermore,

anti-cancer drugs tend to be more toxic to proliferative tumor cells than to non-dividing cells [45]. Consequently, an evaluation of how well a pre-clinical model replicates the proliferative characteristics of the tumor is crucial for effective drug screening and therapy development. Here we showed that monolayer (2D) cultures of meningiomas exhibit a higher Ki-67 index, likely due to the favorable in vitro environment compared to primary tumors [46]. In contrast, our 3D model showed a similar Ki-67 index (with proliferating cells evenly distributed throughout

the samples) that more closely mimicked the corresponding primary tumors, corroborating the results described by Yamazaki et al. [30], who utilized similar culture conditions to ours. We have previously experienced this elevation of 2D proliferation in an in vivo model, where the animal tumors resembled their corresponding primary patient-derived tumor [32]. This also suggests our 3D cell model has a greater likeness to in vivo than to 2D and could function as a bridge between 2D and in vivo [47]. To maintain intra-patient 3D model consistency and cellular heterogeneity, we used third-passage cells, which in our previous study retained stem cell-related biomarker-positive cells, thus preserving stem cell-like features from benign meningiomas [32]. Passaging cells sacrifices some morphological consistency, however, such as the absence of fibrous tissue observed in the primary tumors, in exchange for improved uniformity across the 3D models. Prospectively, we will explore different cell passage stages (passage 0, 1, and 3) to optimize the balance between consistency and cellular diversity.

Copy number variations were similar for all samples but tended towards a lower signal intensity, especially for the MO-42 sample. We hypothesize the meddling of a competing cell type such as the fibroblast, which is common in meningiomas [7] and meninges [48] may be influencing results. Similar findings have been reported in pancreatic organoid cultures using a similar method with Matrigel, where fibroblast growth could be visualized [49]. Yamazaki et al. [30] found comparable copy number variations between primary and organoid culture at low passages but found few chromosomal changes when performing long-term cultures. These findings highlight the importance of validating patient-derived models' likeness to corresponding primary tumors before using them as pre-clinical models.

Using BrainClassifier v12.8, all samples were classified within the meningioma methylation class, with a tendency toward similar subclasses in most cases. One sample (MO-39 – WHO grade 2) showed an insignificant match with the Intermediate A subclass for the primary tumor and a benign subclass for the corresponding 3D model. Sahm et al. (2017) [12] reported discrepancies between the then used WHO classification and DNA methylation-based classification. Furthermore, BrainClassifier does not provide information on which specific CpG sites the classifier emphasizes within each class.

Epigenetically, we observed a high degree of congruency in DNA methylation patterns across all five tumor/3D model pairs. When assessing hypo- and hypermethylated CpG sites, we found a strong correlation between the CpG methylation levels in primary tumors and their corresponding 3D models ($R > 0.95$, $p \leq 2.22 \times 10^{-16}$). This was even higher than that reported for our in vivo models ($R = 0.82-0.93$) [32], likely

influenced by the mixture of rodent DNA in the stroma [50]. The findings in the 3D models align with those of Yamazaki et al. [30], who reported high epigenetic congruency in low-passage organoids. Additionally, when examining the top 1000 most variant CpG sites, four of the pairs still clustered with their corresponding samples, further emphasizing their similarity.

We identified DMPs that were hypomethylated in the 3D models compared to the primary patient-derived tumors, indicating a possible loss of tumor-specific methylation patterns in a few genomic locations. After statistical adjustments, no significantly differentially methylated probes were found between the 3D models and their corresponding primary tumors, supporting their similarity. The lack of statistical significance does not rule out the possibility of real biological differences, however, warranting caution in the interpretation of these results. While there was a high correlation of the methylation levels between 3D models and the primary tumors, which increases the model's relevance for studying tumor biology, the methylation changes could indicate potential deviations from the behavior of the primary tumor due to the lack of microenvironment influences. The hypomethylated pathways, including those related to cytoskeletal dynamics and cell motility, extracellular matrix (ECM) remodeling, and particularly cell-cell and cell-matrix interactions, may reflect cellular adaptation to the simplified artificial culture environment, which lacks the complex signaling of the in vivo tumor microenvironment [51]. Moreover, the hypomethylation of developmental pathways also suggests that cells in the 3D model regain plasticity, indicative of adaptation to in vitro conditions. This plasticity enables cells to adjust their phenotype and behaviors to meet the environmental challenges posed by 3D culture. As is common with in vitro cultures, these conditions often mimic stress or wound-like environments, which facilitates an increased "healing" response due to mechanical disruption or the absence of a supportive microenvironment.

Although 3D models represent a significant advancement over traditional 2D models, they still highlight some well-known limitations of in vitro modeling [52] such as the interaction with the tumor microenvironment, which could potentially be addressed by co-culturing the 3D models with components of the in-situ tumor microenvironment [53]. This approach requires further investigation in future studies.

Methodological limitations

In addition to the limited number of samples, this study has several limitations. First, establishing in vitro models is challenging due to cellular senescence, particularly in primary cells with limited division potential that enter replicative senescence rapidly after few passages. This

is evident in benign meningiomas [54], where low proliferation and reduced telomerase activity cause rapid senescence, limiting cell expansion and long-term culture [55–57]. We observed that fresh third-passage cells had a 100% success rate in forming 3D models in hydrogel, while cryopreserved third-passage cells used at the sixth passage had a 0% success rate. The three-month incubation period required to develop 3D models could potentially delay drug testing assignments for meningiomas. However, the growth of these tumors is generally not as time-sensitive for treatment decisions. For the more time-sensitive malignant subtype, we demonstrate that 3D model development can be achieved in just a few weeks. Prospectively, it will be important to assess various incubation periods, such as one and two months, for benign tumors.

Furthermore, extraction from VitroGel was difficult with the benign and atypical cells and resulted in fragmented samples, an issue we did not observe with the malignant cells (IOMM-Lee). Matrigel allows easier extraction for benign samples [30, 31] but has batch variability and undefined composition, which can skew results [58]. In contrast, xeno-free VitroGel provides batch consistency for more homogenous experiments.

Moreover, DNA methylation analysis of FFPE tissue can be affected by DNA damage from the fixation process, potentially leading to inaccurate bisulfite conversion and overestimation of methylation [59]. This may contribute to discrepancies between FFPE (primary tumors) and fresh frozen samples (3D models) in our study. However, we applied a heating step (90°C for 60 min) during DNA extraction to reduce this bias (see Supplemental Material 2). Previously applying this step has shown to minimize differences between FFPE and frozen samples [59].

Conclusions

Despite a few pattern deviations, our patient-derived 3D models replicated the primary meningiomas in terms of cell morphology, immunohistochemistry, and epigenetic features. The overall cytoarchitecture of meningioma subtypes, particularly the fibrous tissue and collagen components, was not retained in the 3D models. 3D models provide a cost-effective and accessible alternative to in vivo models that is more accurate than monolayer 2D models in mimicking primary tumors, particularly in terms of proliferation indices. These results suggest that our 3D model shows promise for large-scale screening of potential treatments, both novel and approved, that are tailored to individual patient characteristics. This approach could benefit meningioma patients who require additional treatment beyond surgery, including those with subtotal resections, atypical or malignant tumors, or where surgery is not advisable and only biopsy

is available. Further studies are necessary to identify and match effective drugs on a personalized, tumor-specific basis and to determine their suitability for specific meningioma subgroups in clinical applications.

Abbreviations

2D	Two-Dimensional
3D	Three-Dimensional
ARRIVE	Animal Research: Reporting of In Vivo Experiments
ATCC	American Type Culture Collection
BP	Biological Process (from Gene Ontology)
BRIDGE	Brain Research-Inter Disciplinary Guided Excellence
CBTRUS	Central Brain Tumor Registry of the United States
CNS	Central Nervous System
CNV	Copy Number Variation
CP	Cerebellopontine
CRL	Charles River Laboratories
DMSO	Dimethyl Sulfoxide
DMEM	Dulbecco's Modified Eagle Medium
DNA	Deoxyribonucleic Acid
DMP	Differentially Methylated Probe
ECM	Extracellular Matrix
EMA	Epithelial Membrane Antigen
EPIC	Infinium MethylationEPIC BeadChip
FBS	Fetal Bovine Serum
FFPE	Formalin-Fixed Paraffin-Embedded
FDR	False Discovery Rate
GOBP	Gene Ontology Biological Process
GOCC	Gene Ontology Cellular Component
GOMF	Gene Ontology Molecular Function
GSEA	Gene Set Enrichment Analysis
H&E	Hematoxylin & Eosin
IDAT	Illumina DNA Array Technology File Format
IOMM	Lee-A specific malignant meningioma cell line
KEGG	Kyoto Encyclopedia of Genes and Genomes
MNG	Meningioma
MO	Meningioma Odense (Sample Identifier)
MsigDB	Molecular Signatures Database
NF2	Neurofibromatosis Type 2
NGS	Next-Generation Sequencing
PBS	Phosphate-Buffered Saline
PCR	Polymerase Chain Reaction
PCA	Principal Component Analysis
PID	Pathway Interaction Database
PR	Progesterone Receptor
PRISMA	Preferred Reporting Items for Systematic Reviews and Meta-Analyses
RNA	Ribonucleic Acid
SNP	Single Nucleotide Polymorphism
SSTR2	Somatostatin Receptor Type 2
T1	weighted-A type of MRI sequence
TME	Tumor Microenvironment
WHO	World Health Organization

Supplementary Information

The online version contains supplementary material available at <https://doi.org/10.1186/s40478-025-02008-w>.

Supplementary Material 1. Immunohistochemistry scoring

Supplementary Material 2. Examples of images and staining scores

Supplementary Material 3. Morphological descriptions

Supplementary Material 4. DNA methylation step-by-step protocol

Supplementary Material 5. Animal experiment subpart

Supplementary Material 6. Scoping review protocol

Supplementary Material 7. First search string

Supplementary Material 8. Repeat search string

Supplementary Material 9. DNA quality

Supplementary Material 10. Heatmap on all 5 pairs

Supplementary Material 11. DMP probes for all samples at 0.2 and 0.4 cut off with gene annotation

Supplementary Material 12. GSEA top 20 pathways

Acknowledgements

We address a special thanks to biomedical laboratory technician Helle Wohlleben for invaluable assistance in preparing samples and performing sections and immunohistochemical stainings, and biomedical laboratory technician Mirjeta Krasniqi for helping with performing EPICv2 935k on all samples. We also thank the staff at Department of Neurosurgery for active participation in tissue handling. Finally, we thank Claire Gudex, MBChB, MD, University of Southern Denmark, for final proofreading.

Author contributions

MSA: conceptualization, methodology, in vitro and in vivo experimental parts, systematic scoping review subpart, methodology, figures, and tables and analyses and interpretation of all data; AYN: in vitro experimental part, systematic scoping review subpart; JKP and MW: assessment of primary tumors, xenografts, 2D and 3D cell model morphology and immunohistochemical staining; CLP, AC, GH, HBB and MWM: DNA methylation analyses and interpretation; BBO: methodology and in vitro study part; FRP: conceptualization, methodology. MSA, AYN, MW, JKP, MWM, CLP, AC, GH, TM, CAP, BBO, HBB, CBP, BH and FRP performed review, wrote, edited, and approved the final draft.

Funding

Open access funding provided by University of Southern Denmark MSA received funding from Danish 3R-Center. The funder had no part in the design, analyses, or reporting of the study.

Data availability

Most data generated or analyzed during this study are included in this published article (and its Supplemental Material files). The remaining datasets generated during and/or analyzed during the current study are available from the corresponding author on reasonable request. The digital histology and immunohistochemistry files and the IDAT files generated and analyzed are not publicly available due to large file sizes, but they are available from the corresponding author on reasonable request.

Declarations

Ethics approval and consent to participate

The study was approved by the Regional Committees on Health Research Ethics for Southern Denmark (S-20190105). All participants signed consent forms. The animal protocol was submitted to and approved (29th August 2019) by the Danish Animal Experiments Inspectorate (2019-15-0201-00195). The full approved protocol (in Danish) can be provided upon reasonable request.

Consent for publication

All patients involved in the project have signed a regionally approved consent form.

Competing interests

The authors declare no competing interests.

Author details

¹Department of Neurosurgery, Odense University Hospital, Odense, Denmark

²Department of Clinical Research, University of Southern Denmark, Odense, Denmark

³BRIDGE (Brain Research - Inter Disciplinary Guided Excellence), University of Southern Denmark, Odense, Denmark

⁴Department of Nuclear Medicine, Department of Clinical Research, Odense University Hospital, Odense, Denmark

⁵Department of Pathology, University Hospital of Southern Denmark, Esbjerg, Denmark

⁶Department of Regional Health Research, University of Southern Denmark, Odense, Denmark

⁷Department of Pathology, Odense University Hospital, University of Southern Denmark, Odense, Denmark

⁸Department of Neurosurgery, Henry Ford Health, Detroit, MI, USA

⁹Michigan State University, East Lansing Michigan, USA

¹⁰Department of Neurosurgery, Rigshospitalet, Copenhagen, Denmark

¹¹Department of Clinical Medicine, University of Copenhagen, Copenhagen, Denmark

¹²Department of Clinical Neuroscience, Karolinska Institute, Stockholm, Sweden

¹³Department of Surgical Pathology, Zealand University Hospital, Roskilde, Denmark

Received: 3 March 2025 / Accepted: 13 April 2025

Published online: 24 April 2025

References

- Goetz LH, Schork NJ (2018) Personalized medicine: motivation, challenges, and progress. *Fertil Steril* 109(6):952–963
- Dasgupta K, Jeong J (2019) Developmental biology of the meninges. *Genesis* 57(5):e23288
- Ostrom QT, Price M, Neff C, Cioffi G, Waite KA, Kruchko C et al (2022) CBTRUS statistical report: primary brain and other central nervous system tumors diagnosed in the united States in 2015–2019. *Neuro Oncol* 24(Suppl 5):v1–v95
- Ostrom QT, Price M, Neff C, Cioffi G, Waite KA, Kruchko C et al (2023) CBTRUS statistical report: primary brain and other central nervous system tumors diagnosed in the united States in 2016–2020. *Neuro Oncol* 25(12 Suppl 2):iv1–iv99
- Klaeboe L, Lonn S, Scheie D, Auvinen A, Christensen HC, Feychting M et al (2005) Incidence of intracranial meningiomas in Denmark, Finland, Norway and Sweden, 1968–1997. *Int J Cancer* 117(6):996–1001
- Deltour I, Johansen C, Auvinen A, Feychting M, Klaeboe L, Schuz J (2009) Time trends in brain tumor incidence rates in Denmark, Finland, Norway, and Sweden, 1974–2003. *J Natl Cancer Inst* 101(24):1721–1724
- Louis DN, Perry A, Wesseling P, Brat DJ, Cree IA, Figarella-Branger D et al (2021) The 2021 WHO classification of tumors of the central nervous system: a summary. *Neuro Oncol* 23(8):1231–1251
- Bhat AR, Wani MA, Kirmani AR, Ramzan AU (2014) Histological-subtypes and anatomical location correlated in meningeal brain tumors (meningiomas). *J Neurosci Rural Pract* 5(3):244–249
- Nigim F, Wakimoto H, Kasper EM, Ackermans L, Temel Y (2018) Emerging medical treatments for meningioma in the molecular era. *Biomedicines*;6(3)
- Bi WL, Mei Y, Agarwalla PK, Beroukhir R, Dunn IF (2016) Genomic and epigenomic landscape in meningioma. *Neurosurg Clin N Am* 27(2):167–179
- Suppiah S, Nassiri F, Bi WL, Dunn IF, Hanemann CO, Horbinski CM et al (2019) Molecular and translational advances in meningiomas. *Neuro Oncol* 21(Suppl 1):i4–i17
- Sahm F, Schrimpf D, Stichel D, Jones DTW, Hielscher T, Schefzyk S et al (2017) DNA methylation-based classification and grading system for meningioma: a multicentre, retrospective analysis. *Lancet Oncol* 18(5):682–694
- Choudhury A, Magill ST, Eaton CD, Prager BC, Chen WC, Cady MA et al (2022) Meningioma DNA methylation groups identify biological drivers and therapeutic vulnerabilities. *Nat Genet* 54(5):649–659
- Driver J, Hoffman SE, Tavakol S, Woodward E, Maury EA, Bhavne V et al (2022) A molecularly integrated grade for meningioma. *Neuro Oncol* 24(5):796–808
- Wang JZ, Nassiri F, Mawrin C, Zadeh G (2023) Genomic landscape of meningiomas. *Adv Exp Med Biol* 1416:137–158
- Wang JZ, Nassiri F, Aldape K, von Deimling A, Sahm F (2023) The epigenetic landscape of meningiomas. *Adv Exp Med Biol* 1416:175–188
- Wang JZ, Landry AP, Raleigh DR, Sahm F, Walsh KM, Goldbrunner R et al (2024) Meningioma: international consortium on meningiomas (ICOM) consensus review on scientific advances & treatment paradigms for clinicians, researchers, and patients. *Neuro Oncol*

18. Goldbrunner R, Stavrinou P, Jenkinson MD, Sahm F, Mawrin C, Weber DC et al (2021) EANO guideline on the diagnosis and management of meningiomas. *Neuro Oncol* 23(11):1821–1834
19. Voss KM, Spille DC, Sauerland C, Suero Molina E, Brokinkel C, Paulus W et al (2017) The Simpson grading in meningioma surgery: does the tumor location influence the prognostic value? *J Neurooncol* 133(3):641–651
20. Shahbandi A, Shah DS, Hadley CC, Patel AJ (2023) The role of pharmacotherapy in treatment of meningioma: A systematic review. *Cancers (Basel)*;15(2)
21. Andersen MS, Kofoed MS, Paludan-Muller AS, Pedersen CB, Mathiesen T, Mawrin C et al (2023) Meningioma animal models: a systematic review and meta-analysis. *J Transl Med* 21(1):764
22. Kapalczyńska M, Kolenda T, Przybyła W, Zajczkowska M, Teresiak A, Filas V et al (2018) 2D and 3D cell cultures - a comparison of different types of cancer cell cultures. *Arch Med Sci* 14(4):910–919
23. Gunti S, Hoke ATK, Vu KP, London NR (2021) Jr. Organoid and spheroid tumor models: techniques and applications. *Cancers (Basel)*;13(4)
24. Simian M, Bissell MJ, Organoids (2017) A historical perspective of thinking in three dimensions. *J Cell Biol* 216(1):31–40
25. Lancaster MA, Knoblich JA (2014) Organogenesis in a dish: modeling development and disease using organoid technologies. *Science* 345(6194):1247125
26. Drost J, Clevers H (2018) Organoids in cancer research. *Nat Rev Cancer* 18(7):407–418
27. Clevers H (2016) Modeling development and disease with organoids. *Cell* 165(7):1586–1597
28. Jacob F, Salinas RD, Zhang DY, Nguyen PTT, Schnoll JG, Wong SZH et al (2020) A Patient-Derived glioblastoma organoid model and biobank recapitulates Inter- and Intra-tumoral heterogeneity. *Cell* 180(1):188–204e22
29. Kim J, Koo BK, Knoblich JA (2020) Human organoids: model systems for human biology and medicine. *Nat Rev Mol Cell Biol* 21(10):571–584
30. Yamazaki S, Ohka F, Hirano M, Shiraki Y, Motomura K, Tanahashi K et al (2021) Newly established Patient-derived organoid model of intracranial meningioma. *Neuro Oncol*
31. Chan HSC, Ng HK, Chan AK-Y, Cheng SH, Chow C, Wong N et al (2021) Establishment and characterization of meningioma patient-derived organoid. *J Clin Neuroscience: Official J Neurosurgical Soc Australasia* 94(dpi):192–199
32. Andersen MS, Halle B, Wrenfeldt M, Petersen JK, Møller MW, Jurmeister P et al (2024) Orthotopic meningioma rat model exhibits morphological and immunohistochemical congruency and epigenetic concordance with benign primary patient-derived tumors. *Sci Rep* 14(1):31933
33. Lee WH (1990) Characterization of a newly established malignant meningioma cell line of the human brain: IOMM-Lee. *Neurosurgery* 27(3):389–395 discussion 96
34. Percie du Sert N, Ahluwalia A, Alam S, Avey MT, Baker M, Browne WJ et al (2020) Reporting animal research: explanation and elaboration for the ARRIVE guidelines 2.0. *PLoS Biol* 18(7):e3000411
35. Tricco AC, Lillie E, Zarin W, O'Brien KK, Colquhoun H, Levac D et al (2018) PRISMA extension for scoping reviews (PRISMA-ScR): checklist and explanation. *Ann Intern Med* 169(7):467–473
36. McHugh ML (2012) Interrater reliability: the kappa statistic. *Biochem Med (Zagreb)* 22(3):276–282
37. Capper D, Stichel D, Sahm F, Jones DTW, Schrimpf D, Sill M et al (2018) Practical implementation of DNA methylation and copy-number-based CNS tumor diagnostics: the Heidelberg experience. *Acta Neuropathol* 136(2):181–210
38. Zhou W, Laird PW, Shen H (2017) Comprehensive characterization, annotation and innovative use of Infinium DNA methylation BeadChip probes. *Nucleic Acids Res* 45(4):e22
39. Gu Z ComplexHeatmap Complete Reference 2022 [Available from: <https://jokergoo.github.io/ComplexHeatmap-reference/book/>]
40. Subramanian A, Tamayo P, Mootha VK, Mukherjee S, Ebert BL, Gillette MA et al (2005) Gene set enrichment analysis: a knowledge-based approach for interpreting genome-wide expression profiles. *Proc Natl Acad Sci U S A* 102(43):15545–15550
41. Illumina Infinium MethylationEPIC v2.0 Product Files 2025 [Available from: <https://support.illumina.com/downloads/infinium-methylationepic-v2-0-product-files.html>]
42. Prasad CP, Tripathi SC, Kumar M, Mohapatra P (2023) Passage number of cancer cell lines: importance, intricacies, and way-forward. *Biotechnol Bioeng* 120(8):2049–2055
43. van de Weijer LL, Ercolano E, Zhang T, Shah M, Banton MC, Na J et al (2023) A novel patient-derived meningioma spheroid model as a tool to study and treat epithelial-to-mesenchymal transition (EMT) in meningiomas. *Acta Neuropathol Commun* 11(1):198
44. Kastan MB, Bartek J (2004) Cell-cycle checkpoints and cancer. *Nature* 432(7015):316–323
45. Hanahan D, Weinberg RA (2011) Hallmarks of cancer: the next generation. *Cell* 144(5):646–674
46. Tonn JC, Ott MM, Bouterfa H, Kerkau S, Kapp M, Muller-Hermelink HK et al (1997) Inverse correlation of cell proliferation and expression of progesterone receptors in tumor spheroids and monolayer cultures of human meningiomas. *Neurosurgery* 41(5):1152–1159
47. Urzi O, Gasparro R, Costanzo E, De Luca A, Giavaresi G, Fontana S et al (2023) Three-Dimensional cell cultures: the Bridge between in vitro and in vivo models. *Int J Mol Sci*;24(15)
48. Dorrier CE, Jones HE, Pintaric L, Siegenthaler JA, Daneman R (2022) Emerging roles for CNS fibroblasts in health, injury and disease. *Nat Rev Neurosci* 23(1):23–34
49. Ehlen L, Arndt J, Treue D, Bischoff P, Loch FN, Hahn EM et al (2020) Novel methods for in vitro modeling of pancreatic cancer reveal important aspects for successful primary cell culture. *BMC Cancer* 20(1):417
50. Lin MT, Tseng LH, Kamiyama H, Kamiyama M, Lim P, Hidalgo M et al (2010) Quantifying the relative amount of mouse and human DNA in cancer xenografts using species-specific variation in gene length. *Biotechniques* 48(3):211–218
51. Heredia-Mendez AJ, Sanchez-Sanchez G, Lopez-Camarillo C (2023) Reprogramming of the Genome-Wide DNA methylation landscape in Three-Dimensional Cancer cell cultures. *Cancers (Basel)*;15(7)
52. Katt ME, Placone AL, Wong AD, Xu ZS, Searson PC (2016) Vitro tumor models: advantages, disadvantages, variables, and selecting the right platform. *Front Bioeng Biotechnol* 4:12
53. Gu Z, Wu Q, Shang B, Zhang K, Zhang W (2024) Organoid co-culture models of the tumor microenvironment promote precision medicine. *Cancer Innov* 3(1):e101
54. Baia GS, Slocum AL, Hyer JD, Misra A, Sehati N, VandenBerg SR et al (2006) A genetic strategy to overcome the senescence of primary meningioma cell cultures. *J Neurooncol* 78(2):113–121
55. Puduvalli VK, Li JT, Chen L, McCutcheon IE (2005) Induction of apoptosis in primary meningioma cultures by Fenretinide. *Cancer Res* 65(4):1547–1553
56. Ikeda K, Saeki Y, Gonzalez-Agosti C, Ramesh V, Chiocca EA (1999) Inhibition of NF2-negative and NF2-positive primary human meningioma cell proliferation by overexpression of Merlin due to vector-mediated gene transfer. *J Neurosurg* 91(1):85–92
57. Shu J, Lee JH, Harwalkar JA, Oh-Siskovic S, Stacey DW, Golubic M (1999) Adenovirus-mediated gene transfer of dominant negative Ha-Ras inhibits proliferation of primary meningioma cells. *Neurosurgery* 44(3):579–587 discussion 87–8
58. Passaniti A, Kleinman HK, Martin GR (2022) Matrigel: history/background, uses, and future applications. *J Cell Commun Signal* 16(4):621–626
59. Wen X, Jeong S, Kim Y, Bae JM, Cho NY, Kim JH et al (2017) Improved results of LINE-1 methylation analysis in formalin-fixed, paraffin-embedded tissues with the application of a heating step during the DNA extraction process. *Clin Epigenetics* 9:1

Publisher's note

Springer Nature remains neutral with regard to jurisdictional claims in published maps and institutional affiliations.